

Grid-Supporting Inverters With Improved Dynamics

Sayed Ali Khajehoddin^{ID}, Senior Member, IEEE, Masoud Karimi-Ghartemani^{ID}, Senior Member, IEEE, and Mohammad Ebrahimi^{ID}, Student Member, IEEE

Abstract—A new inverter control approach, called enhanced virtual synchronous machine (eVSM), is proposed based on the VSM concept. Unlike existing VSM approaches, the eVSM does not emulate the rotating inertia based on an assumption of the unlimited energy storage, but it deploys the physically existing inertia of the dc-link element. The eVSM adopts an innovative way of enlarging the inertia utilization range, which obviates the need for having a large dc-link element or a dedicated battery storage system, while still providing the same inertia response of an equivalent synchronous machine. Theoretical developments and numerical results presented in this paper confirm that the proposed eVSM can present a stabilizing support to the grid similar to a synchronous machine despite the small size of its dc-link element. Moreover, its transient responses can be improved beyond those of conventional synchronous machines thanks to the possibility of more flexibly adjusting damping and governor functions.

Index Terms—Distributed generation, grid support, microgrid, photovoltaic (PV), renewable energy, small dc-link capacity, virtual inertia, virtual synchronous machine.

I. INTRODUCTION

INTEGRATION of distributed and renewable energy sources, such as photovoltaic (PV) and wind energy systems, requires intelligent and efficient inverters that offer advanced functionalities, such as standalone (SA) and grid-connected (GC) operation, seamless transition between these modes, and grid-supporting and grid-stabilizing functions both during steady state and transient conditions.

The majority of existing renewable inverters are designed to operate in parallel with the grid. They feed their harvested power to the grid while complying with the grid codes in terms of quality of their generated current. Some of the smarter types of such inverters can also feed or absorb reactive power and

Manuscript received October 10, 2017; revised December 31, 2017, February 20, 2018, April 10, 2018, and May 17, 2018; accepted May 30, 2018. Date of publication July 4, 2018; date of current version December 28, 2018. (Corresponding author: Mohammad Ebrahimi.)

S. A. Khajehoddin and M. Ebrahimi are with the Department of Electrical and Computer Engineering, University of Alberta, Edmonton, AB T6G 1H9, Canada (e-mail: khajeddin@ualberta.ca; m.ebrahimi@ualberta.ca).

M. Karimi-Ghartemani is with the Department of Electrical and Computer Engineering, Mississippi State University, Starkville, MS 39759 USA (e-mail: karimi@ece.msstate.edu).

Color versions of one or more of the figures in this paper are available online at <http://ieeexplore.ieee.org>.

Digital Object Identifier 10.1109/TIE.2018.2850002

can also ride through the transient grid faults and grid frequency swings. Current-controlled (CC) inverters can efficiently control current and ride through the grid faults, but they have issues with operating in the SA mode and/or weak grid conditions due to the fact that their control is directed toward the current [1].

Voltage-controlled (VC) inverters based on the concept of droop characteristics, inspired from the operation principles of synchronous generators (SG), have also been lately developed for inverters [2], [3] to overcome some of the shortcomings of the CC inverters. The VC inverters generally offer a direct voltage support and they can work in both GC and SA modes with minor adjustments (such as virtual impedance and self-synchronizing scheme). However, they need additional logics to ensure the inverter current transients as well as its magnitude during voltage sag remain within acceptable limits.

High penetration level of renewable sources into the existing power system also demands their static and dynamic behaviors to be supportive and stabilizing to the grid. It is commonly stated, for example, that the PV inverters do not have a physical inertia and do not respond to the grid transients in a stabilizing way similar to an SG. Dynamic performance of an SG is such that it naturally releases (or absorbs) inertia power during grid transients leading to improved stability. During a transient increase in the grid's active power, its frequency goes up. This leads to the increase in the SG's rotor speed as these two are coupled. This results in the SG absorbing some of the excess power and storing it as kinetic energy into its rotor mass. Conversely, when there is a shortage in the grid's active power and its frequency falls, the rotor speed decreases and releases some of its kinetic energy into the grid. In addition to this interesting inertial behavior of the SG, its governor and exciter control systems respond to longer-term transients of the grid in a similar stabilizing way because they simply adopt and modify a similar inertia nature into their logic.

Due to such properties of the SG, the concept of the virtual synchronous machine (under various names such as VSM, VISMA, synchronverter, etc.) has been introduced [4]–[10] which intends to reproduce the same dynamics of the SG in an inverter. The VSM methods model the inertia effect using a virtual inertia concept and build it inside their controller. The inverter that uses a VSM will then reproduce that inertia response. This approach implies that the inverter has access to a source of power that can actually supply that inertia. That source is either a battery storage system (BSS), a large dc-link element, the kinetic energy of the wind turbine etc.

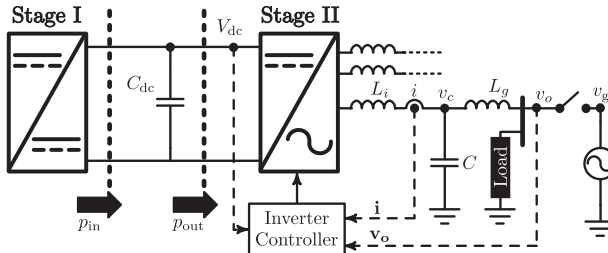


Fig. 1. General block diagram of a double-stage inverter.

Although VSM methods control the inverter as a voltage source, analogies in the operation principles of CC inverters and SGs are also studied in the literature. Xiong *et al.* [11] develop a model for GC inverters based on the principles of SGs. However, this model makes two important implicit assumptions as follows. First, the phase-locked loop (PLL) model is not included. Second, the phasor domain power equations are considered for the instantaneous power. Therefore, more detailed study of such analogy still needs research.

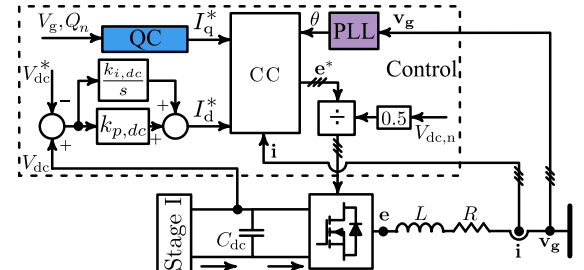
In an inverter, where a BSS or a large dc element is not present, the existing VSM methods cannot successfully work to their promise. The method of [12] adds a control of the dc-link voltage for bidirectional dc/ac converters and HVdc applications while it still assumes a virtual inertia in the controller. This is a contradictory approach since it is not clear whether the dc voltage controller determines the inertia response or the VSM controller.

Implementing VSM for a double-stage inverter (without a BSS or a large capacitor) requires a dc bus voltage controller coupled with an inertia controller that reflects the physical constraints (such as its size and voltage) associated with the bus capacitor. This is clear by considering the system block diagram as shown in Fig. 1. This figure shows a single-line diagram of a three-phase double-stage system [13]. Stage I normally harvests the maximum power called the maximum power point tracking (MPPT). Stage II is an inverter to harvest the energy from the intermediate dc-bus capacitor C_{dc} and deliver it to supply a local load and/or to be injected into the grid.

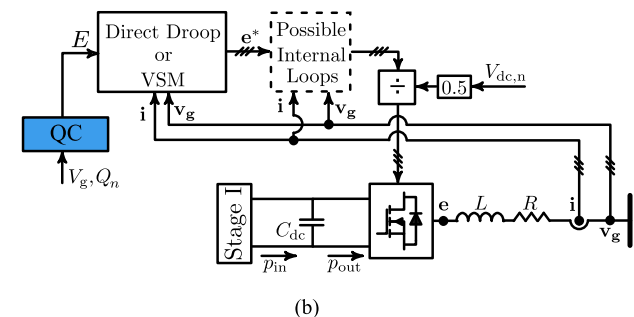
Control of a double-stage inverter is investigated in this paper. A simple yet effective method of controlling the inverter is proposed that is directly inspired from the SG model, thus presenting the closest dynamic performance to an SG. In this method, the rotor inertia is implemented using the intermediate dc-link capacitor, and its speed is mimicked with the capacitor voltage V_{dc} . By allowing the dc-link voltage to change within an enlarged yet admissible range and mapping it into the controller as the internal frequency, it is shown that the proposed method does not require a BSS nor a large capacitor to emulate the rotor inertia. The self-synchronizing property is achieved and improved stability margins, beyond those of synchronous machines, is made possible.

II. COMMON INVERTER CONTROL METHODS

In general there are two different approaches to design control systems for inverters namely current control and voltage



(a)



(b)

Fig. 2. General block diagram. (a) Current-based controllers. (b) Voltage-based controllers.

control methods. In current control methods, a current-control loop based on a feedback of the output current is used, where the reference for the loop is formed based on a PLL that operates on the output voltage. In voltage control methods, the reference for the voltage is generated based on either the droop principles or VSM approaches. In these methods, additional internal loops may or may not exist. Details are explained in the rest of this section.

A. Current Control Approaches

A block diagram of a commonly used current controller (CC) is shown in Fig. 2(a) [14]. The converter of Stage I regulates the input power (p_{in}) and forwards it to the intermediate bus capacitor. A proportional–integral (PI) controller regulates the dc bus voltage and generates the active current reference value (I_d^*). The reactive current reference (I_q^*) in this scheme is determined by the reactive power control (QC) block. These reference currents are then controlled by the CC block. CC could be implemented with two well-known methods, PI controllers in rotating frame and proportional resonant (PR) controllers in the stationary frame. In this figure, $\sin(\theta) = [\sin(\theta) \ \sin(\theta - \frac{2\pi}{3}) \ \sin(\theta + \frac{2\pi}{3})]$ and $\cos(\theta) = [\cos(\theta) \ \cos(\theta - \frac{2\pi}{3}) \ \cos(\theta + \frac{2\pi}{3})]$, which are the in-phase and quadrature-phase signals of the grid voltage from the PLL. The output reference voltage e^* from CC is then divided by half of the dc-link nominal voltage ($V_{dc,n}/2$), forming the modulation index for inverter switches. Although the block diagrams of Fig. 2(a) are drawn for a three-phase system, similar controller structures can be used for a single-phase double stage inverter [15], [16]. The inverter controllers of Fig. 2(a) are limited to operate the inverter in the GC mode because they need an already established voltage.

B. Voltage Control Approaches

Voltage control approaches can be categorized into two wide groups, namely direct droop-based methods and VSM methods as discussed below in more details. General block diagram of such methods is shown in Fig. 2(b).

1) Direct Droop-Based Methods: In the direct droop method, the voltage reference is generated based on the amplitude (V) and frequency (ω) which are obtained from $\omega = \omega_n + k_p(P_n - P)$ and $V = V_n + k_q(Q_n - Q)$, where ω_n and V_n are the nominal grid voltage frequency and amplitude, P_n and Q_n are the nominal active and reactive power, and k_p and k_q are the active and reactive power droop coefficients. Active power (P) and reactive power (Q) are averaged values, which are calculated from the output voltage and current signals and low-pass filters. Close correspondence between this method and VSM approach is shown in [17].

2) Virtual Synchronous Machines: SG is the well-established type of the generator in the existing power system, where its natural and controlled properties have been extensively studied. Attractive properties of the SGs may be summarized as follows.

- 1) SG is primarily a voltage source and can establish a voltage.
- 2) Mechanical speed and electrical frequency are directly coupled and synchronized. This leads to the possibility of interconnecting SGs to form a stable grid.
- 3) Kinetic energy of the rotor acts as a stabilizing inertia during transients.
- 4) Droop-based governor and excitation (or automatic voltage regulator (AVR)) controllers make the SG respond efficiently to output power variations, while maintaining the frequency and voltage within acceptable limits.

Due to these properties, the concept of VSM has been developed (in slightly varying formats) in order to furnish an inverter with appropriate control systems such that it can display the SG properties at operation. Ideally, a VSM can also offer improved stability margins compared to the reference SG thanks to software and thus flexible implementation of dampers.

a) Overview of SG Principles: Circuit diagram and an equivalent model of the SG is presented in Fig. 3(a). According to a rotor speed (or frequency) drooping characteristics, the governor adjusts the flow of the input mechanical power into the machine. The machine converts this power to an output electrical power. According to a voltage magnitude droop characteristics, the exciter adjusts the current into the field winding of the machine, which in turn adjusts the delivered reactive power of the machine. The internally induced voltage in Fig. 3(a) is shown by e with magnitude E and angle θ , where $\theta = \frac{n_p}{2}\theta_m$ and n_p is the number of pole pairs and θ_m is the mechanical angle of the rotor.

The damper windings are located on the rotor to stabilize the machine during transients and disturbances. In a simplified form, governing electromechanical (also called the swing) equation of an SG is expressed as

$$J \frac{d\omega_m}{dt} + D' (\omega_m - \omega_g) = \tau_m - \tau_e \quad (1)$$

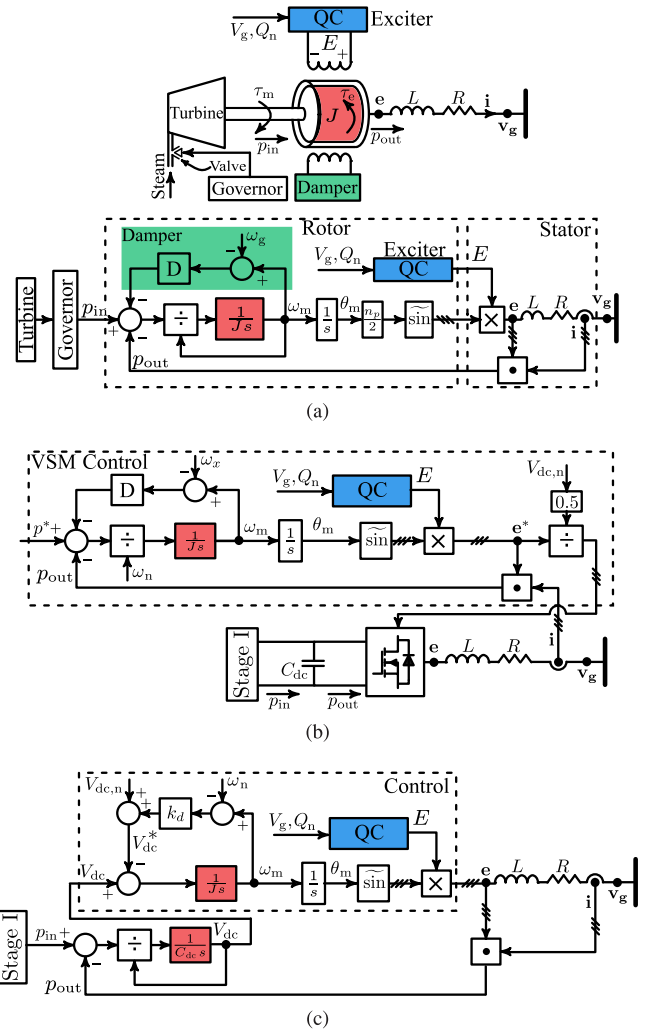


Fig. 3. Block diagram of (a) SG and its model, (b) virtual synchronous machine, and (c) VSM applied to a two-stage converter.

where J denotes the moment of inertia of the rotor mass, τ_m and τ_e are the mechanical and electrical torque on the shaft, ω_g is the grid frequency, and ω_m is the rotor electrical speed (a two-pole machine is considered for simplicity). The term $D'(\omega_m - \omega_g)$ in this equation is a simplified model of the damper winding, where D' is the damping torque coefficient. Considering p_{in} and p_{out} as the input and output powers and noting $(\tau_m - \tau_e)\omega_m = p_{in} - p_{out}$, (1) can be expressed as

$$J\omega_m \frac{d\omega_m}{dt} + D(\omega_m - \omega_g) = p_{in} - p_{out} \quad (2)$$

where $P_{dmp} = D(\omega_m - \omega_g)$ models the damper windings in terms of power instead of torque [18], where D is the damping power coefficient. This is the common, albeit not the unique, way of modeling the damper windings without engaging the circuit level equations of those windings.

As it can be observed in Fig. 3(a), ω_m is the rotor speed and the frequency of the machine's internal voltage e . The rotor speed ω_m becomes equal to ω_g in the steady state in a stable grid. The interaction between the internal voltage and the grid

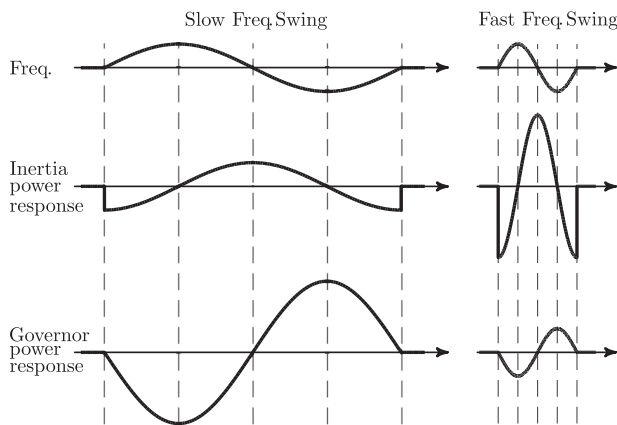


Fig. 4. Distinction between inertia and governor power responses to different grid frequency swings.

voltage via the machine's total equivalent inductance generates the output current.

There are two different types of dynamics in swing equation (2). The input power p_{in} is adjusted by the governor whose bandwidth is small in the range of 0.3–3 Hz and the inertia behavior is represented by the term $J\omega_m\dot{\omega}_m$ whose dominant frequency range is 3–30 Hz [19]. The governor response is proportional to $\omega_n - \omega_m$ and the inertia response is proportional to $-\dot{\omega}_m$. As it is shown in Fig. 4, these two powers will behave differently in response to a grid frequency swing at different rates. Since the governor is slow, its response to low-frequency swings is more dominant than the natural inertia response of the rotor. Conversely, when a quick swing happens, the rotor inertia response is more dominant than the governor response. This is shown by size of the responses in Fig. 4. It is worthwhile noting that the distinction between these two behaviors must be taken into consideration when a VSM intends to fully mimic an SG in order to be able to be fully compatible with the existing grid and be smoothly integrated.

b) Overview of VSM Control Approach: Model of a typical VSM approach is shown in Fig. 3(b). It is clearly observed that the VSM copies the SG principles to a large extent. The QC block in the VSM is equivalent to the exciter of an SG that controls the internal voltage amplitude. There are critical aspects related to the damping and inertia properties of the existing VSMs as discussed below.

1) Damper Winding Emulation Methods: The damper winding is not easy to be emulated. The point denoted by ω_x needs to be exactly equal to the grid frequency. In [8], the measured grid frequency is used and the interaction between the frequency estimation dynamics and the VSM could be an issue specially in weak grid situations and in fast frequency changing conditions. In [5], the nominal value of the grid frequency is used and thus unlike the SG, in this approach the output of the damper model generates a steady-state power when a frequency offset exists. In [20], a transfer function $f(s)$ is applied to $\dot{\omega}_m$ to provide this damping. In [21], a first-order low-pass filter is used for $f(s)$. The advantage of the methods based on

$\dot{\omega}_m$ is that they do not need a grid frequency measurement. However, such methods totally alter the swing equation and they must be carefully designed (if possible at all) so as not to alter its desired response properties. In [9] and [10], another approach is used which is equivalent to adding the derivative of power as the damping term. This is from the same nature of what is also presented in [22] and is shown to offer improved damping properties.

- 2) *Virtual Inertia Implementation:* The “virtual” moment of inertia is given by J . This implies that the system is physically able to supply this level of inertia. In other words, there is an implicit assumption that the system is equipped with adequate storage being in the form of battery, capacitor, rotating inertia such as wind, or a combination of multiple sources.
- 3) *Governor Implementation:* To accurately mimic SG, for a fast disturbance in the grid frequency in the frequency range of the inertia, the input power p_{in} which is controlled by the governor should be almost constant. Otherwise, the dynamics of the input power will interfere with the inertia and the system dynamics will deviate from an SG. The existing VSMs appear to overlook this fact and they do not exactly mimic the inertia dynamics of an SG as they do not model the dynamics of the governor.
- 4) *VSM Implementation for Two-Stage Converters:* The power source can be implemented using a battery where there is no need for extra dc bus control block diagram and no extra dynamics due to the bus capacitor. In this case, the overall VSM behavior is identical to an SG if the governor and damper dynamics are also accurately modeled. The VSM controller in this case is as shown in the dotted box of Fig. 3(b) and as the dc bus voltage is almost constant, no dynamics is imposed from the dc bus capacitor. However, when a VSM approach is used for power sources where a two-stage power converter is needed (such as PV), the dc bus controller and bus capacitors have to be designed such that they do not add significant dynamics to the already achieved dynamics of an SG. In some approaches, such as [12], [23], dc bus controller is added into the VSM method whose equivalent control block diagram is shown in Fig. 3(c). As it can be observed, these methods calculate the dc bus reference voltage V_{dc}^* based on the internal frequency of the VSM. The difference between V_{dc} and V_{dc}^* is then fed to the virtual inertia emulation block ($\frac{1}{J_s}$) to generate the internal frequency. It is clear from this figure that capacitor dynamics in these methods are added to the dynamics of the $\frac{1}{J_s}$ block from the original VSM. These two dynamics are highlighted in red. This extra dynamic from the dc-link capacitor appears as an outer loop with respect to the internal VSM loop. Thus it should be much slower not to alter the VSM dynamics, which demands an excessively large capacitor compared to the emulated inertia. This setup will completely alter the dynamics of the system and deviates from the original VSM if the dc-bus capacitor is not “very large.”

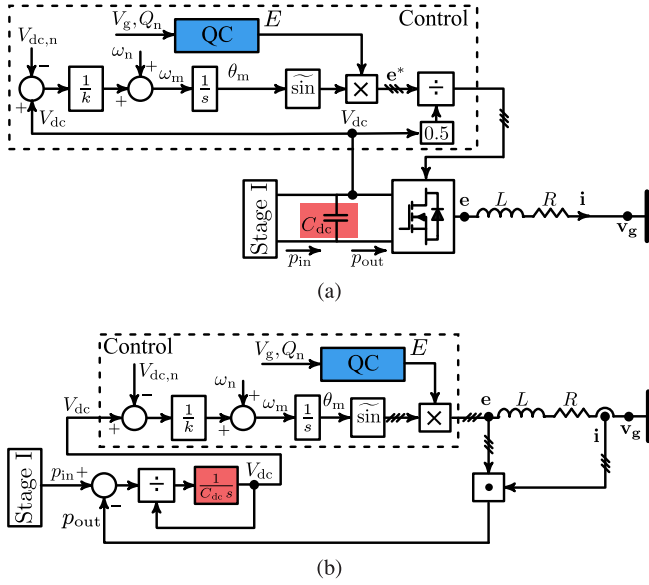


Fig. 5. Block diagram of the proposed (a) converter and controller and (b) overall equivalent model.

III. PROPOSED CONTROLLER

The VSM approach with ideal input power source and with proper governor and damper models can reproduce a virtual inertia behavior with the moment of inertia J . This is implemented by the integrator $\frac{1}{J_S}$ inside the VSM controller. As it was mentioned, when the existing VSM is applied to a converter with bus capacitor and its related controller, the incurred additional dynamics will deviate the emulated system from the targeted SG dynamics and its correct inertia response. It should be noticed that in an SG, J corresponds to the physical rotor mass. By comparing

$$p_{in} - p_{out} = J\omega_m \dot{\omega}_m \quad , \quad p_{in} - p_{out} = C_{dc}V_{dc} \dot{V}_{dc} \quad (3)$$

it can be immediately observed that the bus capacitor in a two stage inverter relates to the rotor mass in the SG. Therefore, there is actually no need for additional integrator to emulate the J as the C_{dc} in the hardware itself will emulate this inertia properly. This is the starting point to derive the proposed controller for a double-stage inverter.

There needs to be a correspondence between the couplet (J, ω_m) and (C_{dc}, V_{dc}) . The proposed method uses a linear transformation as shown in Fig. 5(a), which is expressed by

$$\omega_m = \omega_n + \frac{1}{k}(V_{dc} - V_{dc,n}). \quad (4)$$

It is proved in Section III-C that this choice results in a moment of inertia equal to $J = k(\frac{V_{dc,n}}{\omega_n})C_{dc}$. As demonstrated in Fig. 5(b), the dc-link capacitor dynamics becomes identical to that of the rotor inertia in an SG. Rest of the system is identical to the SG, where ω_m is used to generate inverter voltage with the amplitude coming from QC block. This voltage along with the grid voltage determine the inverter current passing through the filter's impedance. Therefore, the proposed method directly

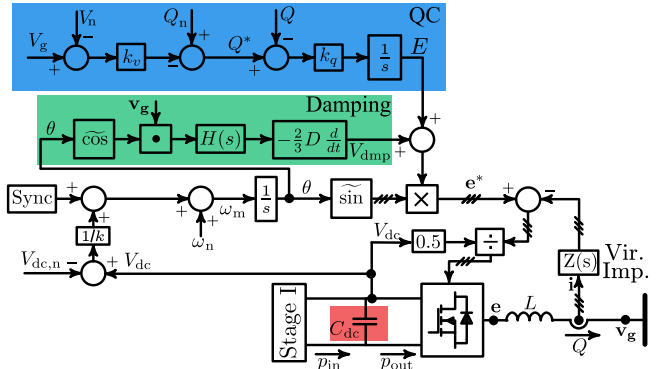


Fig. 6. Detailed block diagram of the proposed controller with all auxiliary control blocks.

integrates the physical inertia coming from the dc bus capacitor. This is in contrast to the existing VSM methods where inertia is implemented inside the controller and duplicates that of the dc-link capacitor.

It is also worth noticing that as V_{dc} is linked to the output frequency in the proposed controller, the bus voltage will vary with the grid frequency. Therefore, the modulation index is scaled using the actual V_{dc} value (not nominal value) to decouple the dc-link voltage variations from the smooth and sinusoidal output voltage [24].

The complete block diagram of the proposed eVSM controller with detailed auxiliary blocks are shown in Fig. 6. As it can be observed, the concept of virtual impedance $[Z(s)]$ can also be introduced to the proposed technique to provide a desired impedance at the output of the inverter. In the simplest form, $Z(s)$ is a gain that represents a virtual resistance that enables achieving desirable stability margins without using physical resistors. It is also worth noting that the proposed method does not need any PLL or any other measurement from the output angle or frequency.

A. Damping Strategy

The SG damping term in the swing equation (2), $P_{dmp} = D(\omega_m - \omega_g)$, should also be added to the proposed controller. Unlike the VSM methods, however, the point of applying P_{dmp} is not available in the proposed controller because the inertia-generating integrator is not inside the controller but rather in the actual system. So P_{dmp} has to be applied differently.

The proposed damping scheme is shown in Fig. 6, in which P_{dmp} is translated into voltage amplitude, namely V_{dmp} , and is implemented at the output of the QC block. In Fig. 6

$$V_{dmp} = -\frac{2}{3}D \frac{d}{dt}(\tilde{\cos}\theta \cdot \mathbf{v}_g) = -DV_g \frac{d}{dt}[\sin(\theta_g - \theta)] \approx -DV_g(\omega_g - \omega_m) \cos(\theta - \theta_g) \quad (5)$$

where V_g is the grid voltage amplitude. This introduces a damping effect in the voltage magnitude E , which translates into P_{dmp} . It is worth noting that in this method the term $(\omega_g - \omega_m)$ is calculated instantaneously with no dynamics without directly measuring or calculating ω_g . Also, as time derivatives are sensitive to the noise in the system, a simple first-order low-pass

filter, shown as $H(s)$ in the diagram, is used on the derivative input signal to block the noise.

B. Reactive Power Control

The QC block controls the reactive power flow according to the voltage magnitude the same way an SG exciter does. The adopted voltage droop controller is given by

$$Q^* = Q_n - k_v(V_g - V_n), \dot{E} = k_q(Q^* - Q). \quad (6)$$

The calculated reactive power reference Q^* from (6) is then used to obtain the desired internal voltage amplitude E , the same way as popular VSM methods such as [5], [10]. The reactive power Q can be calculated using internal voltage variable according to $Q = -E\cos\theta \cdot \mathbf{i} = -E\cos\theta i_a - E\cos(\theta - \frac{2\pi}{3})i_b - E\cos(\theta + \frac{2\pi}{3})i_c$ and the voltage amplitude V_g is calculated according to $V_g = \sqrt{\frac{2}{3}(v_a^2 + v_b^2 + v_c^2)}$ or any other methods to estimate reactive power and voltage magnitude.

In addition, the SG's internal voltage amplitude is proportional to its rotational speed. However, if the machine is equipped with an AVR and reactive power/voltage amplitude droop controller, this dependency is eventually eliminated as the machine's voltage amplitude is determined according to the droop settings. This is the reason that the internal voltage amplitude in the proposed controller does not depend on the rotational speed and is controlled only through the QC block.

C. Self-Synchronization Prior to Grid Connection

Synchronization ensures smooth transition to the GC mode. The method of [9] and [10] is modified and used in this paper. In this method, a cross product of the grid voltage and inverter voltage

$$\begin{aligned} \text{Sync} &= \left(\mu_1 + \frac{\mu_2}{s} \right) (v_{o\alpha}v_{g\beta} - v_{o\beta}v_{g\alpha}) \\ &= \left(\mu_1 + \frac{\mu_2}{s} \right) V_o V_g \sin(\phi_g - \phi_o) \end{aligned} \quad (7)$$

is added as shown in Fig. 6, in which α and β indices denote the variables transformed to $\alpha\beta$ domain by the Clarke transformation and V_o is the output voltage amplitude and ϕ_g and ϕ_o are the grid and output voltage phase angles. μ_1 and μ_2 in (7) are proportional and integral gains of the PI controller, respectively. The signal Sync in (7) is an index of synchronization, which is used to synchronize the inverter output voltage \mathbf{v}_o to grid voltage \mathbf{v}_g prior to connecting to the grid. Prior to the grid connection, due to the correspondence between the active power and ω_m , the signal Sync will be adjusted so that ϕ_g and ϕ_o become equal. At this time, grid connection switch can be closed. Subsequently, $\mathbf{v}_o = \mathbf{v}_g$ and the signal Sync will reset to zero.

D. Inertia Amplification and Energy Storage Minimization

In the proposed eVSM controller, the internal frequency and the dc-link voltage are coupled through (4). There are two key points to this relationship: First, the dc-link voltage is shaped to follow the grid frequency because the internal frequency has to closely follow the grid frequency; and second, the dc-link

voltage will satisfy $\dot{V}_{dc} = k\dot{\omega}_m$ which can be shown to amplify the inertia utilization. To clarify the second point, note that the center dc-link voltage is $V_{dc,n} = k_o\omega_n$. Then, the inertia power of the proposed PV system is equal to

$$\begin{aligned} C_{dc}V_{dc}\dot{V}_{dc} &\approx C_{dc}V_{dc,n}\dot{V}_{dc} = C_{dc}k_o k\omega_n\dot{\omega}_m \\ &\approx (C_{dc}k_o k)\omega_m\dot{\omega}_m = J\omega_m\dot{\omega}_m \end{aligned}$$

where

$$J = (k_o k)C = KC. \quad (8)$$

Equation (8) signifies an *inertia utilization amplification* with gain $K = k_o k$. The first gain k_o depends on the value of the center dc-link voltage $V_{dc,n}$. For a 500 V dc-link voltage in a 60 Hz system, for instance, k_o is equal to $\frac{500}{377} = 1.33$. The second gain k depends on the allowable range of swings of the dc-link voltage. In practice, this gain can be selected relatively large without violating the practical constraints of the system. For instance, for a 120 V (rms) line to neutral three-phase grid and a center dc-link voltage of $V_{dc,n} = 500$ V, the physical limitations of the VSC require that the grid peak voltage $120\sqrt{2} \approx 170$ V remain below $\frac{V_{dc,n}}{2} = 250$ V. Even if we leave about 20V margin for this limit, it means that the dc-link voltage can have a dynamic range of ± 60 V around its center value. If the grid frequency range of variations is ± 0.5 Hz, that is ± 3.14 rad/s, this means k is approximately equal to 20. With this set of numbers, the moment of inertia amplification gain K will be about 26.

In conclusion, by allowing the voltage variations on the dc link, the proposed method makes it possible to either reduce the capacitance to achieve a targeted level of inertia or amplify the inertia with the same capacitance value. In other words, to have an inertia level identical to an SG with the moment of inertia of J , the required capacitor size by the proposed inverter is $C = \frac{J}{K}$. This means 26 times improvement in reducing the size of the capacitor for the above system parameters. Alternatively, a designer may not choose to reduce the size of the capacitor but rather amplify the inertia from such capacitor with the proposed method.

It is worth noting that, in general, increasing the nominal voltage of the dc-link capacitor as required by the proposed method could result to an increase in the system cost. However, as the maximum voltage of commercial dc capacitors are discrete with steps of 50 or 100 V, a designer could have already some room for the dc-link voltage to afford the voltage variations of the proposed controller. Moreover, considering the smaller capacitor needed for the proposed controller, it would be possible to design the capacitance and its voltage span optimally with respect to the cost and required inertia.

E. Inertia Energy Source Management

The source of energy to supply the inertia in an SG is dominantly the rotor mass and normally this inertia energy cannot be taken from the input mechanical source as its time constant does not allow it. The proposed controller in this paper made this distinction and follows the same rule and takes the inertia energy from the bus capacitor. However, in cases where the input source time constant allows it, such as the case in PV

or battery sources, the inertia energy can be managed to be partially provided from the input source. Assume that the desired total emulated moment of inertia is J_{total} and the amount of the moment of inertia provided by bus capacitor in the proposed controller is $J = KC$. Therefore, $J_{\text{total}} = J + J_{\text{in}}$, where J_{in} is the moment of inertia supply by the input stage. In this case, the desired swing equation for the system is $p_{\text{in}} - p_{\text{out}} = J_{\text{total}}\omega_m\dot{\omega}_m = J\omega_m\dot{\omega}_m + J_{\text{in}}\omega_m\dot{\omega}_m$. This can be achieved by adding $-J_{\text{in}}\omega_m\dot{\omega}_m$ to the reference of the input power. More details on the implementation of this idea in a PV system is provided in Section III-H.

F. Stability and Design Aspects of eVSM

A stability analysis of the proposed control system is performed in this section and is used for obtaining clear insights into the design of system parameters. Differential equations of the proposed system of Fig. 6 are summarized as

$$\begin{aligned} \dot{W}_{\text{dc}} &= p_{\text{in}} - p_{\text{out}} = p_{\text{in}} - (E + V_{\text{dmp}})i_d \\ \dot{E} &= k_q(Q^* - Q) = k_q(Q^* + Ei_q) \\ \frac{d}{dt}i_d &= -\frac{R}{L}i_d + \frac{1}{L}(E + V_{\text{dmp}}) - \frac{1}{L}V_{gd} + \omega_m i_q \\ \frac{d}{dt}i_q &= -\frac{R}{L}i_q - \frac{1}{L}V_{gq} - \omega_m i_d \\ \dot{\delta} &= \omega_g - \omega_m, \delta = \theta_g - \theta \end{aligned} \quad (9)$$

where $W_{\text{dc}} = \frac{1}{2}C_{\text{dc}}V_{\text{dc}}^2$, the variables are transformed to dq frame using the internal angle θ , and it is assumed that the virtual impedance is equal to R . The damping term is calculated according to $V_{\text{dmp}} = -\frac{2}{3}\frac{D}{\tau s+1}\frac{d}{dt}\mathbf{v}_g \cdot \hat{\cos}\theta = -\frac{2}{3}\frac{D}{\tau s+1}\frac{d}{dt}\left(\frac{3}{2}V_g\sin(\theta_g - \theta)\right) = -\frac{D}{\tau s+1}V_g(\omega_g - \omega_m)\cos\delta$ and the grid voltage dq components are $V_{gd} = V_g\cos\delta$, $V_{gq} = V_g\sin\delta$. We also notice that $\dot{W}_{\text{dc}} = C_{\text{dc}}\dot{V}_{\text{dc}} = C_{\text{dc}}k[V_{\text{dc},n} + k(\omega_m - \omega_n)]\dot{\omega}_m$. Substituting in (9), it is converted to

$$\begin{aligned} \dot{\omega}_m &= \frac{1}{C_{\text{dc}}k} \frac{p_{\text{in}} - Ei_d - V_{\text{dmp}}i_d}{V_{\text{dc},n} + k(\omega_m - \omega_n)} \\ \dot{E} &= k_q(Q^* - Q) = k_q[Q_n + k_v(V_n - V_g) + Ei_q] \\ \dot{\delta} &= \omega_g - \omega_m \\ \dot{i}_d &= -\frac{R}{L}i_d + \frac{1}{L}(E + V_{\text{dmp}}) - \frac{1}{L}V_g\cos\delta + \omega_m i_q \\ \dot{i}_q &= -\frac{R}{L}i_q - \frac{1}{L}V_g\sin\delta - \omega_m i_d \\ \dot{V}_{\text{dmp}} &= -\frac{1}{\tau}V_{\text{dmp}} - \frac{1}{\tau}DV_g(\omega_g - \omega_m)\cos\delta. \end{aligned} \quad (10)$$

Equation set (10) represents a sixth-order nonlinear system with state variables $(\omega_m, E, \delta, i_d, i_q, V_{\text{dmp}})$. For every given set of values of (p_{in}, Q_n) , the equilibrium point of the equations may be derived and used in linear stability analysis using the Jacobian linearization method. Assuming that the grid frequency/voltage is at its rated, i.e., $\omega_g = \omega_n$, $V_g = V_n$, and the equilibrium point is given by $(\omega_g, E_o, \delta_o, i_{do}, i_{qo}, 0)$, the Jacobian matrix (Γ) will

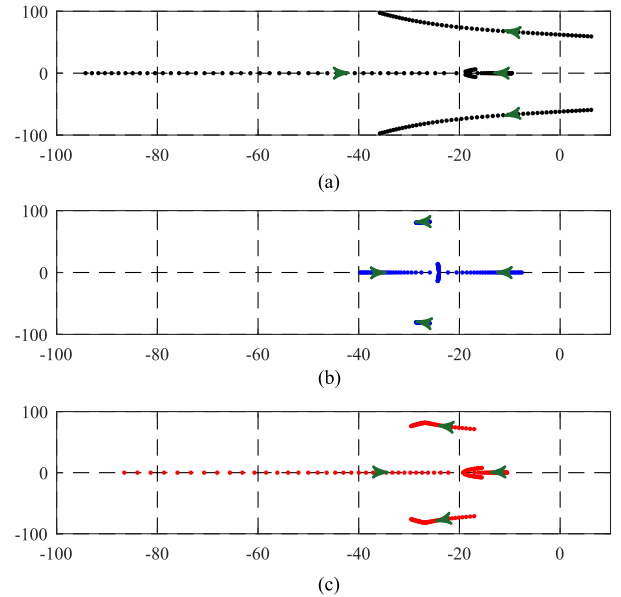


Fig. 7. Loci of dominant eigenvalues of linearized system Γ versus three controller gains. (a) $\beta_1 = 0.75$, $\beta_2 = 0.075$, $D = 0 \rightarrow 0.05$, (b) $\beta_1 = 0.75$, $D = 0.025$, $\beta_2 = 0.05 \rightarrow 0.125$, (c) $D = 0.025$, $\beta_1 = 0.25 \rightarrow 1.25$.

be given by

$$\begin{bmatrix} 0 & -\frac{i_{do}}{C_{\text{dc}}kV_{\text{dc},n}} & 0 & -\frac{E_o}{C_{\text{dc}}kV_{\text{dc},n}} & 0 & -\frac{i_{do}}{C_{\text{dc}}kV_{\text{dc},n}} \\ 0 & k_q i_{qo} & 0 & 0 & k_q E_o & 0 \\ -1 & 0 & 0 & 0 & 0 & 0 \\ i_{qo} & \frac{1}{L} & \frac{V_g}{L}\sin\delta_o & -\frac{R}{L} & \omega_g & 1/L \\ -i_{do} & 0 & -\frac{V_g}{L}\cos\delta_o & -\omega_g & -\frac{R}{L} & 0 \\ \frac{DV_g}{\tau}\cos\delta_o & 0 & 0 & 0 & 0 & -\frac{1}{\tau} \end{bmatrix}.$$

To obtain the equilibrium point, we notice that the first equation implies $E_o i_{do} = p_{\text{in}}$, the second one implies $E_o i_{qo} = -Q_n$, the fourth and fifth equations imply $E_o - Ri_{do} + L\omega_g i_{qo} = V_g \cos \delta_o$ and $L\omega_g i_{do} + Ri_{qo} = -V_g \sin \delta_o$. Thus, $(E_o - Ri_{do} + L\omega_g i_{qo})^2 + (L\omega_g i_{do} + Ri_{qo})^2 = V_g^2$, hence

$$(E_o^2 - Rp_{\text{in}} - L\omega_g Q_n)^2 + (L\omega_g p_{\text{in}} - RQ_n)^2 = V_g^2 E_o^2 \quad (11)$$

which leads to the second-order polynomial versus E_o^2 . Thus, E_o is calculated according to

$$E_o = \sqrt{(A + \frac{1}{2}V_g^2)} + \sqrt{(A + \frac{1}{2}V_g^2)^2 - A^2 - B} \quad (12)$$

$A = Rp_{\text{in}} + L\omega_g Q_n$, $B = (L\omega_g p_{\text{in}} - RQ_n)^2$. By calculating E_o , other variables are obtained from the above relationships.

Three controller parameters are R , D , and k_q . Let us define $R = \beta_1 X$ and $k_q = \beta_2 \frac{\omega_g}{3V_g} X$. These definitions normalize those parameters and facilitates more general design stage. With this definition, our studies show that $0.25 < \beta_1 < 1.25$ and $0.025 < \beta_2 < 0.125$ result in desirable performances. The damping gain D is already normalized. Here, a value between 2 to 5%, i.e., $0.02 < D < 0.05$, is a desired selection. Fig. 7(a) shows the loci of the four dominant eigenvalues of Γ when $\beta_1 = 0.75$, $\beta_2 = 0.075$ and D is varied from 0 to 0.05. The strong stabilizing effect of D is clearly observed from this graph. Fig. 7(b) shows

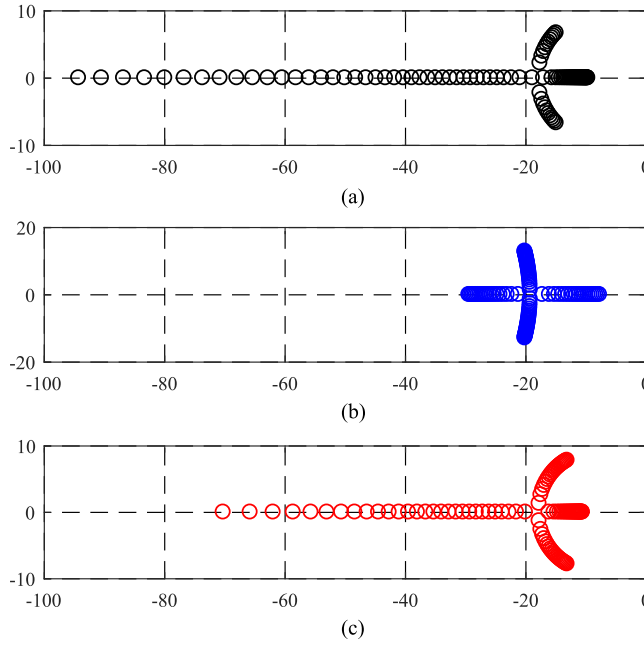


Fig. 8. Loci of dominant zeros of linearized system (input: grid frequency, output: inverter frequency) versus three controller gains. (a) $\beta_1 = 0.75$, $\beta_2 = 0.075$, $D = 0 \rightarrow 0.05$, (b) $\beta_1 = 0.75$, $D = 0.025$, $\beta_2 = 0.05 \rightarrow 0.125$, (c) $D = 0.025$, $\beta_2 = 0.075$, $\beta_1 = 0.25 \rightarrow 1.25$.

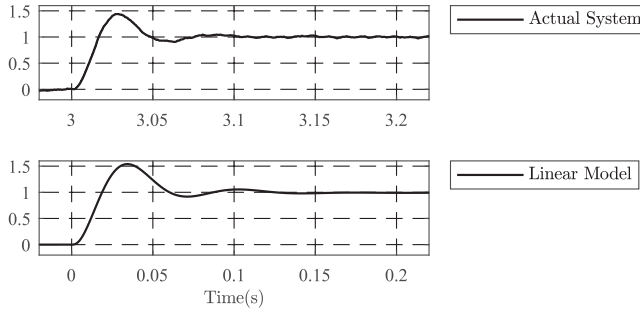


Fig. 9. Small-signal responses of the actual system (top) and zero-pole linear model (bottom) to a grid frequency jump.

the case where $\beta_1 = 0.75$, $D = 0.025$ and β_2 is varied from 0.05 to 0.125. This parameter mainly shifts the AVR and low pass filter real poles. Finally, Fig. 7(c) shows the case where $\beta_2 = 0.075$, $D = 0.025$ and β_1 is varied from 0.25 to 1.25. This is the impact of virtual resistance which will improve all poles. However, excessive increase of this parameter will cause a return of low-frequency complex poles toward the right side. For the results presented in this paper, the values $\beta_1 = 1$, $\beta_2 = 0.1$, $D = 0.03$ are picked which result the location of poles at $-376 \pm j363$, $-32 \pm j89$, $-15 \pm j13$.

The analysis presented above determines the stability of the system and not necessarily reflects a complete picture of the transient responses of the system. The reason is that the analysis is limited to poles and does not consider possible zeros of the system. Fig. 8, for instance, shows the two dominant zeros (out of the total four zeros) when the input and output of the system are defined as the grid frequency ω_g and the VSM frequency ω_m , respectively. The loci of zeros for the same scenarios de-

scribed in Fig. 7 are presented in Fig. 8. For the particular chosen parameters of $\beta_1 = 1$, $\beta_2 = 0.1$, $D = 0.03$, the zeros are at -6465 , -506 , $-14 \pm j11.4$. It is observed that the two dominant zeros are close to two of the dominant poles, i.e., $-15 \pm j13$. Therefore, the system response, as far as this input and output are concerned, are dominantly determined by the two other poles, i.e., $-32 \pm j89$. This is confirmed in Fig. 9 in which the actual system simulation (in PSIM) and the zero-pole model (in MATLAB) response are shown.

The above stability analysis is performed for the GC operation and is only approximately valid for a microgrid situation. A more complete analysis can be performed using existing methods such as [25] for complete eigenvalue and sensitivity analysis in microgrid operation.

Design of synchronization block gains, μ_1 and μ_2 , can be carried out using PLL theory because it is readily observed that the VSM is much similar to a PLL during presynchronization. Therefore, the set of values $(\mu_1 + \frac{\mu_2}{s}) = \frac{1}{V_n^2}(100 + \frac{1}{0.05s})$ is proposed and used in this paper.

G. Stability Analysis for LCL Output Filter

A stability analysis of the proposed control system when the output filter is extended to an *LCL* topology is performed in this section. Similar to the *L* filter case, differential equations of proposed system of Fig. 6 with the *LCL* filter are obtained as

$$\begin{aligned} \dot{\omega}_m &= \frac{1}{C_{dc}k} \frac{p_{in} - Ei_d - V_{dmp}i_d}{V_{dc,n} + k(\omega_m - \omega_n)} \\ \dot{E} &= k_q(Q^* - Q) = k_q[Q_n + k_v(V_n - V_g) + Ei_q] \\ \dot{\delta} &= \omega_g - \omega_m \\ \dot{i}_d &= -\frac{R}{L}i_d + \frac{1}{L}(E + V_{dmp}) - \frac{1}{L}v_{cd} + \omega_m i_q \\ \dot{i}_q &= -\frac{R}{L}i_q - \frac{1}{L}v_{cq} - \omega_m i_d \\ \dot{i}_{gd} &= \frac{1}{L_g}(v_{cd} - V_g \cos \delta) + \omega_m i_{gq} \\ \dot{i}_{gq} &= \frac{1}{L_g}(v_{cq} - V_g \sin \delta) - \omega_m i_{gd} \\ \dot{v}_{cd} &= \frac{1}{C}(i_d - i_{gd}) + \omega_m v_{cq} \\ \dot{v}_{cq} &= \frac{1}{C}(i_q - i_{gq}) - \omega_m v_{cd} \\ \dot{V}_{dmp} &= -\frac{1}{\tau}V_{dmp} - \frac{1}{\tau}DV_g(\omega_g - \omega_m) \cos \delta. \end{aligned} \quad (13)$$

The capacitor voltage of the *LCL* filter is v_c and its capacitance is C . The grid side current is i_g and its inductance is L_g .

Equation set (13) represents a tenth-order nonlinear system with state variables $(\omega_m, E, \delta, i_d, i_q, i_{gd}, i_{gq}, v_{cd}, v_{cq}, V_{dmp})$. Similar to the *L* filter analysis, the Jacobian linearization method can be used. Assuming that the grid frequency/voltage is at its rated, the equilibrium point is given by $(\omega_g, E_o, \delta_o, i_{do}, i_{qo}, i_{gdo}, i_{gqo}, v_{edo}, v_{cqo}, 0)$. To obtain the

equilibrium point, we notice that the equations imply

$$\begin{aligned}
 E_o i_{do} &= p_{in}, \quad E_o i_{qo} = -Q_n \\
 v_{cd0} &= E_o - Ri_{do} + L\omega_g i_{qo} = E_o - (Rp_{in} + L\omega_g Q_n)E_o^{-1} \\
 &= E_o - AE_o^{-1} \\
 v_{cq0} &= -Ri_{qo} - L\omega_g i_{do} = (RQ_n - L\omega_g p_{in})E_o^{-1} = bE_o^{-1} \\
 b &= RQ_n - L\omega_g p_{in} \\
 v_{cd0} + L_g\omega_g i_{gq0} &= \\
 &= V_g \cos \delta_o, \quad v_{cq0} - L_g\omega_g i_{gd0} = V_g \sin \delta_o \\
 i_{gd0} &= i_{do} + C\omega_g v_{cq0} = (p_{in} + C\omega_g b)E_o^{-1} \\
 i_{gq0} &= i_{qo} - C\omega_g v_{cd0} = -C\omega_g E_o - (Q_n - C\omega_g A)E_o^{-1} \\
 &\Rightarrow (v_{cd0} + L_g\omega_g i_{gq0})^2 + (v_{cq0} - L_g\omega_g i_{gd0})^2 = V_g^2 \\
 &\Rightarrow \{(1 - L_g C \omega_g^2)E_o - [A(1 - L_g C \omega_g^2) + L_g \omega_g Q_n]E_o^{-1}\}^2 \\
 &\quad + \{[(1 - L_g C \omega_g^2)b - L_g \omega_g p_{in}]E_o^{-1}\}^2 = V_g^2 \\
 &\Rightarrow \{(1 - L_g C \omega_g^2)E_o^2 - [A(1 - L_g C \omega_g^2) + L_g \omega_g Q_n]\}^2 \\
 &\quad + \{[(1 - L_g C \omega_g^2)b - L_g \omega_g p_{in}]\}^2 = V_g^2 E_o^2 \\
 &\Rightarrow (\gamma E_o^2 - A\gamma - L_g \omega_g Q_n)^2 + (\gamma b - L_g \omega_g p_{in})^2 = V_g^2 E_o^2 \\
 \gamma &= 1 - L_g C \omega_g^2 \\
 &\Rightarrow (E_o^2 - A - L_g \omega_g Q_n \gamma^{-1})^2 + (b - L_g \omega_g p_{in} \gamma^{-1})^2 \\
 &= V_g^2 \gamma^{-2} E_o^2.
 \end{aligned}$$

Comparing with the similar equation we derived for the L filter in (11) and its solution in (12), here the solution will be

$$E_o = \sqrt{\left(\bar{A} + \frac{1}{2}\bar{V}_g^2\right)} + \sqrt{\left(\bar{A} + \frac{1}{2}\bar{V}_g^2\right)^2 - \bar{A}^2 - \bar{B}}$$

where $\bar{V}_g = V_g \gamma^{-1}$, $\bar{A} = A + L_g \omega_g Q_n \gamma^{-1}$, $\bar{B} = (b - L_g \omega_g p_{in} \gamma^{-1})^2$.

By calculating E_o , other variables are obtained from the above relationships. The Jacobian matrix (Γ) will be given by the matrix at the bottom of this page.

Fig. 10 shows the loci of system eigenvalues with LCL filter versus changes in the grid inductance. In this figure, L_g changes

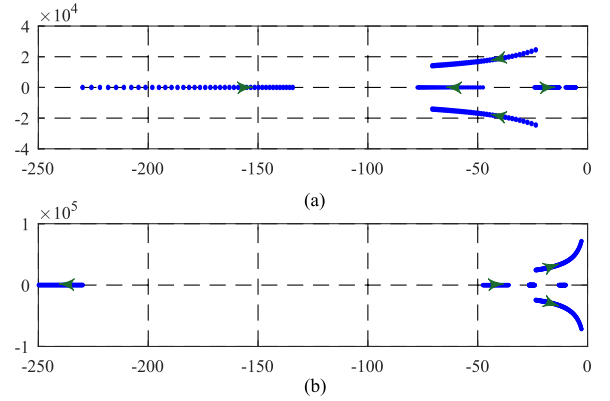


Fig. 10. Loci of eigenvalues of the linearized system Γ with the LCL filter versus grid side inductance variations. (a) L_g varying from 1 to 5 mH, (b) L_g varying from 1 mH to 0.1 mH.

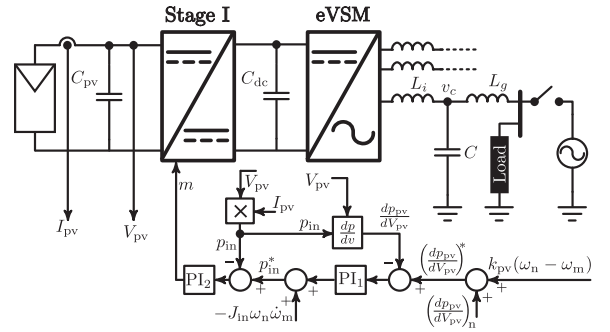


Fig. 11. Proposed method applied to a two-stage PV system.

from 1 to 0.1 mH and from 1 to 5 mH. It can be observed that although L_g changes over a wide range, eigenvalues of the system are not drastically changing and it remains stable. Notice that the decrease in the damping of resonance pole does not cause a problem as it is accompanied with an increase in the resonance frequency [26].

H. Proposed eVSM Applied to Two-Stage PV System

The proposed method can be applied to any two stage converter system. As an example, in this section, the proposed method is applied to a two-stage PV system as shown in **Fig. 11**.

$$\left[\begin{array}{ccccccccc} 0 & -\frac{i_{do}}{C_{dc}kV_{dc,n}} & 0 & -\frac{E_o}{C_{dc}kV_{dc,n}} & 0 & 0 & 0 & 0 & -\frac{i_{do}}{C_{dc}kV_{dc,n}} \\ 0 & k_q i_{qo} & 0 & 0 & k_q E_o & 0 & 0 & 0 & 0 \\ -1 & 0 & 0 & 0 & 0 & 0 & 0 & 0 & 0 \\ i_{qo} & \frac{1}{L} & 0 & -\frac{R}{L} & \omega_g & 0 & 0 & -\frac{1}{L} & 0 \\ -i_{do} & 0 & 0 & -\omega_g & -\frac{R}{L} & 0 & 0 & -\frac{1}{L} & 0 \\ i_{gq0} & 0 & \frac{V_g}{L_g} \sin \delta_o & 0 & 0 & 0 & \omega_g & \frac{1}{L_g} & 0 \\ -i_{gdo} & 0 & -\frac{V_g}{L_g} \cos \delta_o & 0 & 0 & -\omega_g & 0 & 0 & \frac{1}{L_g} \\ v_{cq0} & 0 & 0 & \frac{1}{C} & 0 & -\frac{1}{C} & 0 & 0 & \omega_g \\ -v_{cd0} & 0 & 0 & 0 & \frac{1}{C} & 0 & -\frac{1}{C} & -\omega_g & 0 \\ \frac{D}{\tau} V_g \cos \delta_o & 0 & 0 & 0 & 0 & 0 & 0 & 0 & -\frac{1}{\tau} \end{array} \right].$$

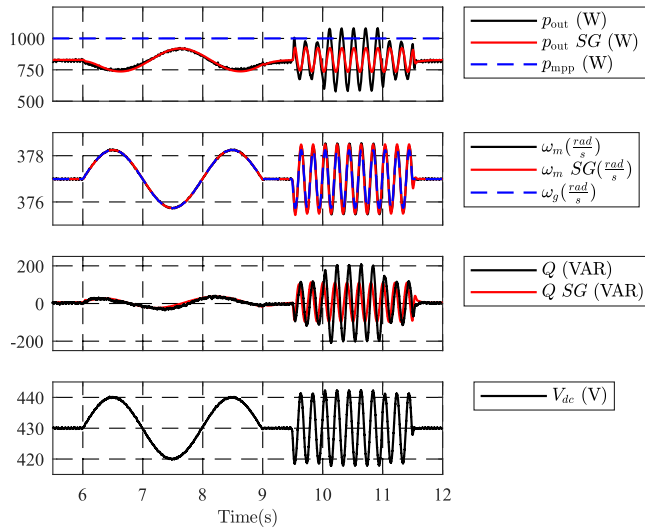


Fig. 12. Simulation results comparing inertial behavior of the proposed controller with SG ($6 < t < 11.5$).

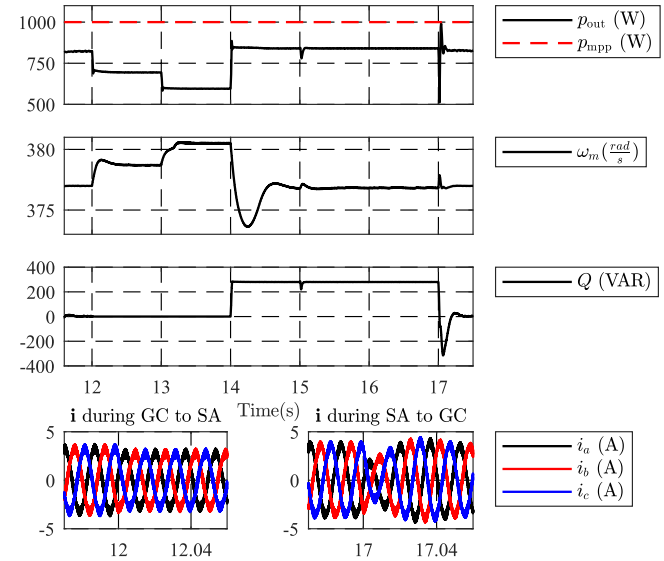


Fig. 14. Simulation results of the proposed controller during SA and transitions between SA and GC ($12 < t < 18$).

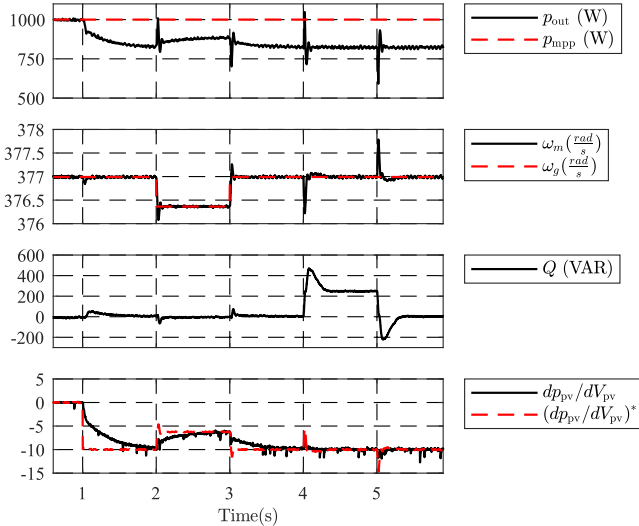


Fig. 13. Simulation results showing performance of the proposed method for input power, grid frequency, and grid amplitude jump ($t < 6$).

One challenge in renewable applications in general is the variability of the input power. In PV systems, it is desirable to operate as close as possible to the unknown maximum power point (MPP) during normal operations. According to the PV characteristic, derivative of the PV output power with respect to its output voltage (i.e., $\frac{dp_{pv}}{dV_{pv}}$) at the MPP is zero. The proposed method of Fig. 11 uses a control loop over the variable $\frac{dp_{pv}}{dV_{pv}}$ to regulate it to $(\frac{dp_{pv}}{dV_{pv}})_n + k_{pv}(\omega_n - \omega_m)$. This mechanism will operate the PV at a point slightly on the right side of the MPP determined by $(\frac{dp_{pv}}{dV_{pv}})_n$ as long as the grid frequency is close to the nominal value. Similar to an SG governor, this loop will adjust the input power according to the droop characteristic (k_{pv}) with respect to the internal frequency variable (ω_m). A first PI_1

TABLE I
SYSTEM PARAMETERS

Dc link nominal voltage	$V_{dc,n}$	430 V
Dc link capacitor	C_{dc}	$880 \mu F$
Grid LN voltage (peak)	V_g	$120\sqrt{2}$ V
Inverter power rating	S	1 kVA
Grid frequency	f	60 Hz
Switching frequency	f_s	10 kHz
Filter Parameters	L_i	5 mH
	C	2 μF

with slow time constant is used to emulate the slow behavior of an SG governor.

As observed in Fig. 11 and according to the discussion in Section III-E, the optional input inertia term ($-J_{in}\omega_m\dot{\omega}_m$) can be added to the input power reference (p_{in}^*) and a fast PI_2 controller is used to allow tracking of power reference up to the desired frequency band of the inertia.

IV. SIMULATIONS AND EXPERIMENTAL RESULTS

Performance of the proposed controller is examined with simulations and a sample of results is presented in this section. System parameters are presented in Table I. The control system parameters are designed based on Section III-F. The proposed controller is simulated in the following scenario:

- 1) $0 < t < 1$: MPPT operation ($\frac{dp_{pv}}{dV_{pv}} = 0$, $P_{mpp} = 1000$ W);
- 2) $t = 1$: $(\frac{dp_{pv}}{dV_{pv}})^*$ jump of -10 ;
- 3) $t = 2$: grid frequency jump of -0.1 Hz;
- 4) $t = 3$: grid frequency jump of 0.1 Hz;
- 5) $t = 4$: grid magnitude jump of -2.5% ;
- 6) $t = 5$: grid magnitude jump of 2.5% ;
- 7) $6 < t < 9$: slow (0.5 Hz) grid freq. swing with 0.2 Hz peak;

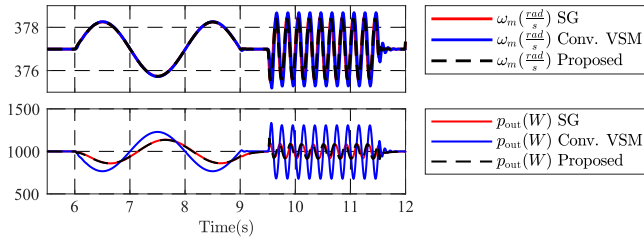


Fig. 15. Comparison of the fast and slow inertial response of the proposed controller and conventional VSM with SG ($6 < t < 11.5$).

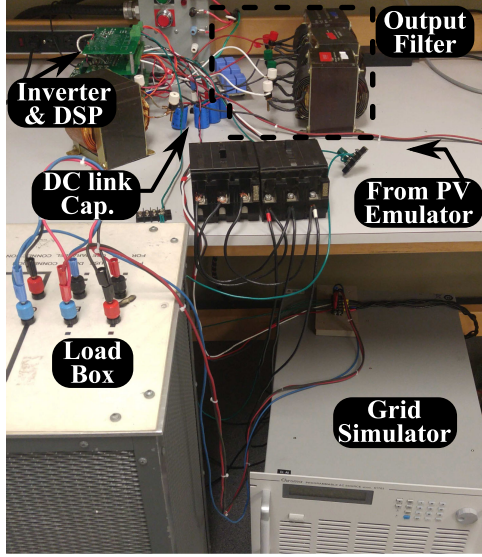


Fig. 16. View of the experimental setup.

- 8) $9.5 < t < 11.5$: fast (5 Hz) grid freq. swing with 0.2 Hz peak;
- 9) $10 < t < 11$: input inertia command enabled;
- 10) $t = 12$: islanding (initial resistive load of 700 W);
- 11) $t = 13$: 100 W load shedding;
- 12) $t = 14$: 255 W/255 Var load addition;
- 13) $t = 15$: presynchronization enabled;
- 14) $t = 17$: reconnection to grid.

As it can be observed, the controller perfectly responds to the grid and its transients in a stabilizing manner and settles in the new operating point. Correspondence between the ω_m and V_{dc} can be seen in this test. It is observed that controller regulates its output power when there is a jump in the input power, while V_{dc} and ω_m return to their steady-state values prior to this jump. The inertia utilization amplification, the inertia source management stage, distinction between the inertia and governor transients, GC and SA operations, and seamless transition between these modes are observed. Fig. 15 also compares the inertial behavior of the proposed method with the conventional VSM of Fig. 3(c) and an SG. As it can be observed, the inertial behavior of the conventional VSM does not match with the SG, while the proposed method perfectly matches with the SG.

The proposed controller is also experimentally validated. In this test, the grid is emulated with a Chroma ac source with 60 V line-to-neutral voltage. A buck converter is implemented as the

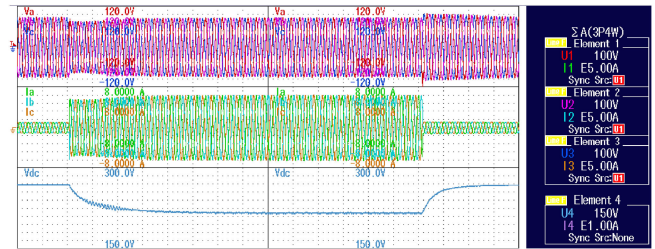
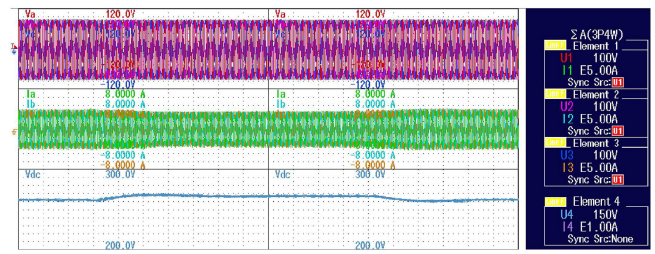
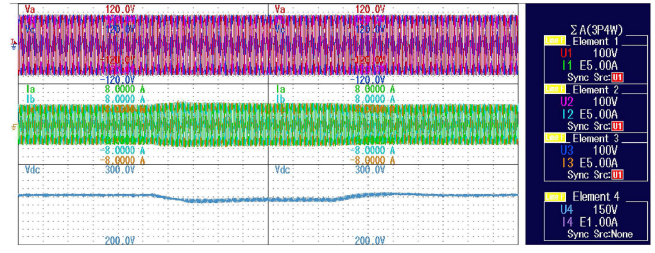


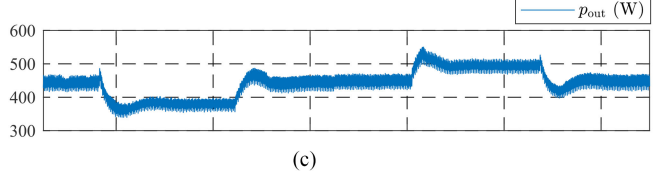
Fig. 17. Experimental results showing the SA load change. Top: inverter LN voltages, middle: inverter currents, bottom: V_{dc} (500 ms/div). Left: Load is increased from 150 to 500 W, Right: load decreased.



(a)



(b)



(c)

Fig. 18. Experimental results showing the grid frequency jump. (a) and (b) Top: inverter LN voltages, middle: inverter currents, bottom: V_{dc} (100 ms/div). $P_{mpp} = 450$ W and f jumps (a) left: 60 Hz to 60.1 Hz, right: 60.1 Hz to 60 Hz, (b) left: 60 Hz to 59.9 Hz, right: 59.9 Hz to 60 Hz, and (c) p_{out} during these jumps.

stage I, which connects a Chroma PV simulator to the inverter's dc link. Controllers for both stage I and the proposed eVSM are implemented on Texas Instrument TMS320F28335 DSP. DC-link center voltage is designed to be at 250 V and other system parameters are presented in Table I. A view of the experimental setup is shown in Fig. 16.

Load jump scenarios are presented in Fig. 17, in which the load in the SA mode jumps from 150 to 500 W and vice versa. DC-link voltage variations in response to the frequency variations are also shown in this figure.

In the results of Fig. 18, the inverter is working in the GC mode, where the grid frequency jumps in the following sequence: from 60 to 60.1 Hz to 60 to 59.9 Hz and back to 60 Hz. It can be observed that the controller reacts to frequency jumps

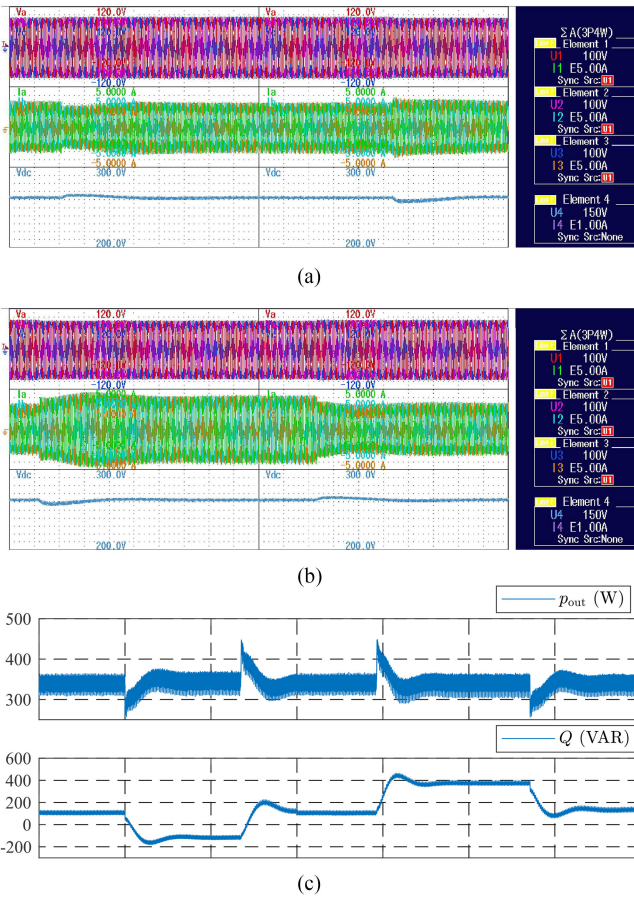


Fig. 19. Experimental results for the grid amplitude jump. (a) and (b) Top: inverter LN voltages, middle: inverter currents, bottom: V_{dc} (100 ms/div), (a) nominal grid 2.5% increase and back to nominal grid (b) nominal grid 2.5% decrease and back to nominal grid right, (c) output active and reactive power.

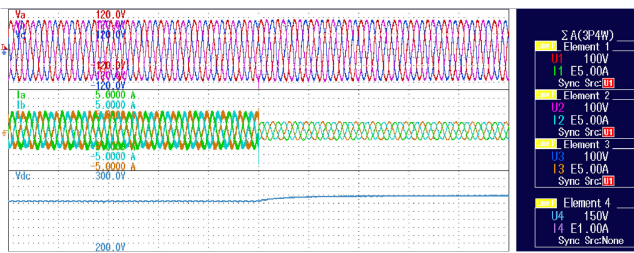


Fig. 20. Experimental results for GC to SA transient. Top: inverter LN voltages, middle: inverter currents, bottom: V_{dc} (50 ms/div).

and the active power as well as the dc-link voltage change accordingly.

Grid voltage amplitude is also changed by $\pm 2.5\%$ and the results are presented in Fig. 19. The change in the output reactive power can be observed in these results.

The proposed controller also provides a seamless transient between SA and GC modes of the operation. The results in Fig. 20 show the inverter voltage and current during a transition from GC to SA mode, where the voltage remains stable and the inverter continues supplying local loads.

V. CONCLUSION

An innovative inverter controller, named eVSM was proposed in this paper. The method was derived to have a similar performance to the SG with the possibility of improved transients and stability as well. The proposed inverter controller uses the physical dc-link capacitor dynamics for inertial response rather than relying on a dedicated battery storage or large dc element. Contrary to the existing VSMs, the eVSM approach does not duplicate the inertia loop inside the controller and directly deploys the energy in the dc-link element. It uses an innovative method to enlarge the range of utilization of this energy. Other auxiliary controllers such as self-synchronization prior to grid connection were also developed and discussed for the proposed method. Numerical results are presented to validate the proposed controller in the context of a two-stage PV inverter application.

REFERENCES

- [1] C. K. Sao and P. W. Lehn, "Control and power management of converter fed microgrids," *IEEE Trans. Power Syst.*, vol. 23, no. 3, pp. 1088–1098, Aug. 2008.
- [2] J. M. Guerrero, P. C. Loh, M. Chandorkar, and T.-L. Lee, "Advanced control architectures for intelligent microgrids, part I: Decentralized and hierarchical control," *IEEE Trans. Ind. Electron.*, vol. 60, no. 4, pp. 1254–1262, Apr. 2013.
- [3] J. C. Vásquez Quintero *et al.*, "Modeling, analysis, and design of stationary reference frame droop controlled parallel three-phase voltage source inverters," *IEEE Trans. Ind. Elect.*, vol. 60, no. 4, pp. 1271–1280, Apr. 2013.
- [4] H.-P. Beck and R. Hesse, "Virtual synchronous machine," in *Proc. 9th Int. Conf. Electric. Power Quality Utilisation*, 2007, pp. 1–6.
- [5] Q.-C. Zhong and G. Weiss, "Synchronverters: Inverters that mimic synchronous generators," *IEEE Trans. Ind. Electron.*, vol. 58, no. 4, pp. 1259–1267, Apr. 2011.
- [6] Q.-C. Zhong, P.-L. Nguyen, Z. Ma, and W. Sheng, "Self-synchronized synchronverters: Inverters without a dedicated synchronization unit," *IEEE Trans. Power Electron.*, vol. 29, no. 2, pp. 617–630, Feb. 2014.
- [7] S. M. Ashabani and Y. A.-r. I. Mohamed, "New family of microgrid control and management strategies in smart distribution grids analysis, comparison and testing," *IEEE Trans. Power Syst.*, vol. 29, no. 5, pp. 2257–2269, Sep. 2014.
- [8] F. Gao and M. R. Iravani, "A control strategy for a distributed generation unit in grid-connected and autonomous modes of operation," *IEEE Trans. Power Del.*, vol. 23, no. 2, pp. 850–859, Apr. 2008.
- [9] M. Karimi-Ghartemani, "Universal integrated synchronization and control for single-phase DC/AC converters," *IEEE Trans. Power Electron.*, vol. 30, no. 3, pp. 1544–1557, Mar. 2015.
- [10] M. Karimi-Ghartemani, S. A. Khajehoddin, P. Piya, and M. Ebrahimi, "Universal controller for three-phase inverters in a microgrid," *IEEE J. Emerg. Select. Topics Power Electron.*, vol. 4, no. 4, pp. 1342–1353, Dec. 2016.
- [11] L. Xiong *et al.*, "Static synchronous generator model: A new perspective to investigate dynamic characteristics and stability issues of grid-tied PWM inverter," *IEEE Trans. Power Electron.*, vol. 31, no. 9, pp. 6264–6280, Sep. 2016.
- [12] M. Ashabani, Y. Abdel-Rady, and I. Mohamed, "Novel comprehensive control framework for incorporating VSCs to smart power grids using bidirectional synchronous-VSC," *IEEE Trans. Power Systems*, vol. 29, no. 2, pp. 943–957, Mar. 2014.
- [13] S. B. Kjaer, J. K. Pedersen, and F. Blaabjerg, "A review of single-phase grid-connected inverters for photovoltaic modules," *IEEE Trans. Ind. Appl.*, vol. 41, no. 5, pp. 1292–1306, Sep./Oct. 2005.
- [14] F. Blaabjerg, R. Teodorescu, M. Liserre, and A. Timbus, "Overview of control and grid synchronization for distributed power generation systems," *IEEE Trans. Ind. Electron.*, vol. 53, no. 5, pp. 1398–1409, Oct. 2006.
- [15] M. Ebrahimi, S. A. Khajehoddin, and M. Karimi-Ghartemani, "Fast and robust single-phase dq current controller for smart inverter applications," *IEEE Trans. Power Electron.*, vol. 31, no. 5, pp. 3968–3976, May 2016.

- [16] S. Khajehoddin, M. Karimi-Ghartemani, A. Bakhshai, and P. Jain, "High quality output current control for single phase grid-connected inverters," in *Proc. 29th Ann. IEEE Appl. Power Electron. Conf. Expo.*, 2014, pp. 1807–1814.
- [17] S. D'Arco and J. A. Suul, "Equivalence of virtual synchronous machines and frequency-droops for converter-based microgrids," *IEEE Trans. Smart Grid*, vol. 5, no. 1, pp. 394–395, Jan. 2014.
- [18] S. D'Arco and J. A. Suul, "Virtual synchronous machines classification of implementations and analysis of equivalence to droop controllers for microgrids," in *Proc. 2013 IEEE Grenoble PowerTech*, 2013, pp. 1–7.
- [19] H. Alatrash, A. Mensah, E. Mark, G. Haddad, and J. Enslin, "Generator emulation controls for photovoltaic inverters," *IEEE Trans. Smart Grid*, vol. 3, no. 2, pp. 996–1011, Jun. 2012.
- [20] Y. Chen, R. Hesse, D. Turschner, and H.-P. Beck, "Comparison of methods for implementing virtual synchronous machine on inverters," in *Proc. Int. Conf. Renew. Energies Power Quality*, 2012, pp. 1–6.
- [21] J. A. Suul, S. D'Arco, and G. Guidi, "Virtual synchronous machine-based control of a single-phase bi-directional battery charger for providing vehicle-to-grid services," *IEEE Trans. Ind. Appl.*, vol. 52, no. 4, pp. 3234–3244, Jul./Aug. 2016.
- [22] S. Dong and Y. C. Chen, "Adjusting synchronverter dynamic response speed via damping correction loop," *IEEE Trans. Energy Convers.*, vol. 32, no. 2, pp. 608–619, Jun. 2016.
- [23] D. Chen, Y. Xu, and A. Q. Huang, "Integration of dc microgrids as virtual synchronous machines into the ac grid," *IEEE Trans. Ind. Electron.*, vol. 64, no. 9, pp. 7455–7466, Sep. 2017.
- [24] S. A. Khajehoddin, M. Karimi-Ghartemani, P. K. Jain, and A. Bakhshai, "Dc-bus design and control for a single-phase grid-connected renewable converter with a small energy storage component," *IEEE Trans. Power Electron.*, vol. 28, no. 7, pp. 3245–3254, Jul. 2013.
- [25] N. Pogaku, M. Prodanovic, and T. C. Green, "Modeling, analysis and testing of autonomous operation of an inverter-based microgrid," *IEEE Trans. Power Electron.*, vol. 22, no. 2, pp. 613–625, Mar. 2007.
- [26] S. G. Parker, B. P. McGrath, and D. G. Holmes, "Regions of active damping control for LCL filters," *IEEE Trans. Ind. Appl.*, vol. 50, no. 1, pp. 424–432, Jan./Feb. 2014.



Sayed Ali Khajehoddin (S'04–M'10–SM'16) received the B.Sc. and M.Sc. degrees in electrical engineering from the Isfahan University of Technology, Isfahan, Iran, in 1997 and 2000, respectively, and the Ph.D. degree in electrical engineering specialized in power electronics and their applications in renewable energy systems from Queens University, Kingston, ON, Canada, in April 2010.

After completing the master's degree, he co-founded a start-up company, which was focused on the development and production of power analyzers and smart metering products used for smart grid applications. For the doctoral research with Queens University, he focused on the design and implementation of compact and durable microinverters for photovoltaic grid-connected systems. Based on this research, Queens University spun off SPARQ systems, Inc., where he was the Lead R&D Engineer; he worked toward the mass production and commercialization of microinverters from 2010 to 2013. In 2013, he was with the Department of Electrical and Computer Engineering, University of Alberta, Edmonton, AB, Canada.

Dr. Khajehoddin is an Associate Editor for the IEEE TRANSACTIONS ON POWER ELECTRONICS, IEEE TRANSACTIONS ON SUSTAINABLE ENERGY, and the *Journal of Emerging and Selected Topics in Power Electronics*.



Masoud Karimi-Ghartemani (M'01–SM'09) received the Ph.D. degree in electrical and computer engineering from the University of Toronto, Toronto, ON, Canada, in 2004.

From 2005 to 2008, he was a Faculty Member with the Department of Electrical Engineering, Sharif University of Technology. He was a member of ePOWER Laboratory, Queens University from 2008 to 2011. Since 2012, he has been an Associate Professor with the Department of Electrical and Computer Engineering, Mississippi State University, Starkville, MA, USA. He works on modeling and control of distributed energy systems at high penetration level. His research interests include power system analysis, stability, and control. His current interests include the integration of distributed and renewable energy systems.



Mohammad Ebrahimi (S'11) received the B.Sc. and M.Sc. degrees from the Isfahan University of Technology, Isfahan, Iran, in 2010 and 2013, respectively, both in electrical power engineering. He is currently working toward the Ph.D. degree in electrical engineering at the University of Alberta, Edmonton, AB, Canada.

His research interests include power electronics applications in power and renewable energy systems and high power density converters.